Nanoscale engagement of immune checkpoint inhibitor PD-L1 in membrane lipid rafts

Martina Ruglioni,[1,¶] Simone Civita,[2,3¶] Tiziano Salvadori,[4] Sofia Cristiani,[4] Vittoria Carnicelli,[4] Serena Barachini,[5] Iacopo Petrini,[5] Alberto Diaspro,[2,6] Paolo Bianchini,[2,6,] Barbara Storti,[7,*] Ranieri Bizzarri[4,7,*] Stefano Fogli,[1] Romano Danesi,[1]

[1]Unit of Clinical Pharmacology and Pharmacogenetics, Department of Clinical and Experimental Medicine, University of Pisa, Pisa, Italy

[2]Department of Mathematical, Physical and Computer Sciences, University of Parma - Parma, Italy

[3]Nanoscopy, CHT, Istituto Italiano di Tecnologia, Via E. Melen 83, 16152 Genova, Italy

[4]Department of Surgical, Medical and Molecular Pathology, and Critical Care Medicine, University of Pisa, Via Roma 65, 56126 Pisa, Italy

[4]General Pathology, Department of Translational Research & New Technologies in Surgery and Medicine, University of Pisa

[6]DIFILAB, Dipartimento di Fisica, Università degli Studi di Genova, Via Dodecaneso 33, 16146 Genova, Italy

[7]NEST, Scuola Normale Superiore and Istituto Nanoscienze-CNR, Piazza San Silvestro 12, 56127 Pisa, Italy

[¶]Martina Ruglioni and Simone Civita contributed equally to this work

*Corrisponding authors: Barbara Storti (barbara.storti@nano.cnr.it), Ranieri Bizzarri (ranieri.bizzarri@unipi.it)

ABSTRACT

We characterized the relationships of PD-L1 with lipid rafts in the plasma membrane by adopting a toolbox of fluorescence microscopy techniques which span different spatial resolutions and ultimately leverage single molecule detection. On account of our interest in novel therapeutic approaches to Non-Small Cell Lung Cancer (NSCLC), we selected the HCC827 as model cell line, because we demonstrated it possesses an abundant plasma membrane expression of PD-L1 while being representative of common mutation of EGFR gene in NSCLC. Our findings visually revealed for the first time that PD-L1 is engaged in the raft regions of the plasma membrane where it arranges as polydisperse nanostructured clusters with <100 nm size. Consistently, raft disruption by cholesterol depletion leads to significant alteration of this morphological pattern. Engagement in rafts may confer PD-L1 specific functions in the context of PD-L1/PD-1 mediated immuno checkpoint and the immuno-oncology strategies to modulate it.

INTRODUCTION

Programmed cell death 1 ligand (PD-L1, CD274, B7-H1) is a key player protein in immune regulation, taking part in one of the most important immune checkpoints of our organism [1]. PD-L1 suppresses T-cell immunity by interacting with specific receptors on T-cells such as PD-1 and CD80. This inhibitory activity unfolds through a complex mechanism that conveys ligand-receptor binding to the silencing of T-cell cytokine production and the induction of anergy and apoptosis [2]. The primary function of immune checkpoints is to maintain the immune homeostasis of the host in physiological conditions [3]. Yet, evasion of the immune system is a hallmark of cancer, which enables cancer cells to escape the attack from immune cells [4]. Accordingly, several types of cancers exploit the PD-L1/PD-1 interaction to mask cell dysregulation from the T-cell recognition, preventing cancer cell apoptosis [5]. This has led in the last few years to the momentous success of cancer immunotherapy, in which inhibitors (mostly monoclonal antibodies) of the PD-L1/PD-1 binding interaction partially restore the T-cell immune activity and lead to the regression of the neoplasia [6]. Unfortunately, for several cancers, most patients do not show durable remission and progressively develop resistance to the checkpoint blockade drugs [7].

Currently, most patients with metastatic non-small cell lung cancer (mNSCLC) are treated with first-line PD-1 or PD-L1 antibodies and some of them have prolonged survival [8]. Otherwise, the preferred initial treatment of epithelial growth factor receptor (EGFR) mutant NSCLC is the use of EGFR tyrosine kinase (TKI) inhibitors, as these patients exhibit poor response to anti-PD-1/PD-L1 treatments. However, acquired drug resistance may limit the long-term efficacy of EGFR TKIs and no further effective treatment options are currently available for these patients [9]. In this context, the full comprehension of the subtle molecular details underlying the activity of the PD-L1/PD-1 immune checkpoint, particularly those related to the structural properties of the two

molecules, appears utterly necessary to provide new rational for the development of 2nd generation checkpoint blockade strategies.

Structurally, PD-L1 is a 40 kDa type-1 transmembrane protein that consists of IgV-like and IgC-like extracellular domains, a hydrophobic transmembrane domain, and a short cytoplasmic tail (cytoplasmic domain, CD) spanning about 30 amino acids [10, 11]. CD is involved in many regulatory pathways of PD-L1. Of particular relevance is the palmitoylation site at residue Cys^{272} [12]. Palmitoylation consists of the covalent attachment of palmitic acid to amino acids (mostly cysteine). This post-translational modification of several membrane proteins is catalyzed by a family of aspartate-histidine-histidine-cysteine (DHHC) acyltransferases. It has been demonstrated that PD-L1 palmitoylation by DHHC3 stabilizes PD-L1 by suppressing CD ubiquitination, which in turn triggers lysosomal degradation of the immune checkpoint ligand [13]. Accordingly, specific mutation of Cys^{272} or inhibition of the palmitoyltransferase was able to restore immune T-cell activity against cancer cells [14]. These findings led to palmitoylation of PD-L1 (and more recently of PD-1) being a new target for immuno-oncology [15, 16].

Yet, palmitoylation of membrane proteins has a widespread role in cell biology to increase their affinity to the lipid raft regions of the plasma membrane (PM) [17-19]. The current model of PM invokes an interlaced combination of liquid-order (L_O, also referred to as ''lipid raft'') and liquid-disorder (L_d) nanophases, enriched respectively in saturated and unsaturated lipids, together with different amounts of cholesterol [20-22]. A continuous exchange of proteins and protein complexes occurs between the two phases, modulated also by the confining action of the cytoskeleton [23]. This paradigm of membrane assembly was proposed to be a crossroad in every membrane process, such as the formation of protein clusters, signal transduction, endocytosis, and cell polarization and motility [23]. Of note, the structure of the raft can be planar (rectilinear) or non-planar (invaginated). Non-planar rafts can be largely identified with caveolar regions of the PM,

flask-like invaginations of the plasma membrane enriched in the protein Caveolin-1 that contribute to several aspects of cell physiology, including signal transduction events and the specialized caveolar endocytosis mechanism [24, 25].

In spite of the relevant role of CD palmitoylation, the actual engagement of PD-L1 in lipid rafts is still obscure. A recent preprint carried out *in vitro* experiments on giant plasma membrane vesicles (GPMV) to determine the partition of PD-L1 into the lipid-ordered microphase [26]. It was found that palmitoylated PD-L1 indeed displays significant affinity to the ordered phase. Yet, the loss of cytoskeletal organization in GPMV prevented a correct assessment of the PD-L1 relationship with nanostructured rafts in the dynamic conditions of the living cell.

In this work, we set out to investigate the PD-L1/raft engagement in cells by a multiscale toolbox of fluorescence microscopy techniques. More specifically, we first leveraged highly sensitive imaging systems such as membrane-targeted Total Internal Reflection Fluorescence (TIRF) microscopy to reveal the actual partition of PD-L1 in raft regions by colocalization measurements with molecular hallmarks of lipid rafts. Then, we characterized the nanoscale morphology of PD-L1 on the PM by using single-molecule localization microscopy (SMLM) according to the dSTORM imaging scheme [27]. dSTORM belongs to the family of super-resolution imaging techniques, which recently revolutionized the fluorescent microscopy scenario enabling in principle diffraction-unlimited resolution [28]. Likewise all SMLM, dSTORM leverages the ability to randomly activate the fluorescent emission of only a small subset of fluorophores, in order to distinguish them spatially. At each time, the few isolated "ON" fluorophores are detected and localized with high precision. The overall image is built-up over time by piling up all the localizations, enabling spatial resolution as low as a few nanometers [27]. Compared to other SMLM, dSTORM has the great advantage of being easily applicable to common immunofluorescence methods [29]. Indeed, our membrane-specific indirect

immunostaining of PD-L1 proved effective in confocal, TIRF, as well as dSTORM conditions.

MATERIALS AND METHODS

Cell culture

EGFR-mutated NSCLC cells (H1975, H3255, H1650, PC9, and HCC827) were cultured at 37°C in the presence of 5% CO_2. in RPMI-1640 medium containing phenol red and supplemented with NaHCO3, L-glutamine, and 1% of sodium pyruvate (Sigma-Aldrich, Darmstadt, Germany), 1% of penstreptomycin (Sigma-Aldrich, Darmstadt, Germany), and 10% of fetal bovine serum (FBS-Sigma-Aldrich, Darmstadt, Germany). For immunostaining, HCC827 cells were seeded ($3x10^5$) in 35 mm glass-bottom dishes (Willco) with 2 ml of culture medium and cultured for 1 day at 37°C.

Transient expression of Caveolin-1-EGFP and GPI-EGFP in HCC827 cells

A solution made up of 1 μL transfection plasmid (Caveolin-1-EGFP or GPI-EGFP, 1 μg/μL) in 100 μL Opti-Mem reduced Serum Medium (Thermofisher) was added to a solution of 3 μL Lipofectamine 2000 (Thermofisher) in 100 μL Opti-Mem. The resulting mix was incubated for 5 minutes at room temperature and then added to HCC827 cells adhered to 35 mm glass bottom Willco dishes (WillCo Wells BV, Amsterdam). Cells were then incubated at 37°C with 5% CO_2 for 48 hours.

Cholesterol depletion

According to the protocol reported in [30], HCC827 cells were incubated with 5 mM methyl-beta-cyclodextrin (MBCD) at 37°C and 5% CO_2 for 1h directly in the Willco dish where they adhered.

Immunostaining of cells

Adhered cells in the Willco dish were fixed with PFA 2% in PBS for 15 min at RT, rinsed three times with PBS, followed by three times with PBS + 0.5% BSA (PBB). Cells were

then maintained for 40 min at RT in 2% BSA in PBS and rinsed three times with PBB. Next, cells were incubated for 1h with rabbit anti-PD-L1 (mAb D8T4X, Cell Signaling, Danvers, Massachusetts) 1/150 in PBB. After rinsing three times with PBB, cells were incubated for 1h with donkey anti-rabbit Alexafluor647-conjugated IgG 1/400 in PBB. Cells were then extensively rinsed with PBS.

Control cells were immunostained as above but no rabbit anti-PD-L1 (primary) mAb was added.

If nuclear staining was needed, immunostained cells were exposed for 5 min to 1 mg/100 ml Hoechst 33342 (Thermo Fisher Scientific, Waltham, Massachusetts) in water.

Flow cytometry

Flow cytometry was carried out by a MACSQuant Flow Cytometer (Miltenyi Biotec instruments, Bergisch Gladbach, Germany). Cells ($5x10^5$) were resuspended in 100 µl MACSQuant running buffer. Cells were then labeled with either (Sample) 1:100 rabbit anti-PD-L1 AlexaFluor647-conjugated mAb (D8T4X, Cell Signaling Technologies) or (Isotype Control) 1:100 rabbit IgG Isotype Control AlexaFluor647-conjugated mAb (DA1E, Cell Signaling Technologies) for 15 min at 4°C. Unlabeled cells were used as autofluorescence (blank) control. After washing to remove the excess unbound antibody, cells were resuspended in 450 µl of the running buffer and filtered to eliminate any aggregates.

A gating strategy, using the forward scatter (FSC-A, referring to cell size) and side scatter (SSC-A, the cytoplasmic content and potential presence of granules) dot plot was carried out to separate living cells from dead cells, debris, or aggregates. Quantification of PD-L1 expression in tested cell lines was carried out by comparing the signals of sample, isotype control, and blank cells. Acquisition was performed collecting 10,000 events that were analyzed by MACSQuant® Flow Cytometer using the MACSQuantify® Software (Miltenyi Biotech). Statistical significance was assessed by the Anova Test with

Bonferroni correction.

Confocal microscopy

Fluorescence was measured by a laser scanning confocal microscope Nikon, Eclipse Ti. Samples were viewed with a 63x Apochromat NA=1.4 oil-immersion objective. Pixel dwell time was adjusted to 1.52 μs and either 512x512 pixel or 1024x1024 images (line scan speed was changed accordingly) were collected (line average factor: 4). The acquisition channels were set as follows: (i) blue (Hoechst 33342): λ_{ex}=405 λ_{em}= 450/50 nm; (ii) green (Alexa488): λ_{ex}=488, λ_{em}= 525/50 nm; and (iii) Far-red (Alexa647): λ_{ex}=640, λ_{em}= Long Pass 650 nm. The pinhole size was set to 1 airy unit (AU) for the FarRed acquisition channel. Images were visualized and processed by the open-source software Fiji (NIH, Bethesda).

Total Internal Reflection Microscopy and colocalization analysis

Imaging in Total Internal Reflection mode (TIRF-M) was carried out by a Leica AF6000 fluorescence microscope equipped with a TIRF-M condenser and 100x oil-immersion objective (NA 1.47). We adjusted the penetration depth of the evanescent wave to 100-150 nm. Fluorescence was recorded by a cooled EM-CCD (Hamamatsu C1900–13). The microscope was equipped with laser lines for excitation of EGFP (488 nm) and AlexaFluor647 (640 nm). Acquisition settings were as in the following:

- Green channel (EGFP): excitation was set to 488 nm, the emission was collected between 520 and 550 nm, and a dichroic filter at 502 nm separated excitation from emission;
- Far-red channel (AlexaFluor647): excitation was set at 640 nm, emission was collected by a superposition of 600/40 641/75 and LP650 filters (yielding light at 604–620 and 650–679 nm), and a dichroic filter at 570 nm separated excitation from

emission;

Colocalization analysis

Functional colocalization of the green and far-red images was quantified by Pearson's coefficient R using the JACoP plugins of Fiji, with automatic thresholding according to Costes et al. [31].

Super-resolution microscope setup and imaging

An N-STORM TIRF microscope (Nikon Instruments) equipped with an oil immersion objective (CFI Apo TIRF 100×, NA 1.49, oil; Nikon) was used to acquire 20,000-80,000 frames with 30 ms acquisition time using TIRF illumination. Excitation intensities after the obejctive were as follows: 35.4 mW for the 647 nm readout (450 mW laser; Nikon Instruments) and 5.5 mW for the 405 activation (450 mW laser; Nikon Instruments). We set a repeating cycle of 1 activation frame at 405 nm / 3 readout frames at 647 nm. Image detection was performed with a cMOS camera (Orca-Flash 4.0 C13440, Hamamatsu). The Perfect Focus System (Nikon) was used during the entire recording process. The fluorescence-emitted signal was spectrally selected by the four-color dichroic mirrors (ZET405/488/561/647; Chroma) and filtered by a quadri bandpass filter (ZT405/488/561/647; Chroma).

For imaging conditions, STORM imaging buffer was used containing a glucose oxidase solution as an oxygen scavenging system. The imaging buffer was prepared as follows. 690 μL of 50 mM Tris buffer (pH 8.0), containing 10 mM of NaCl and 10% w/v of glucose was mixed with 7 μL of GLOX solution, 7 μL of 2-mercaptoethanol. The resulting solution was added to the immunostained cells, and the Willco dish was sealed with parafilm. GLOX solution was composed of glucose oxidase (14 mg) and Catalase (50 uL, 17 mg/mL) dissolved in 200 μL of 10 mM Tris (pH 8.0) + 50 mM NaCl.

Single-molecule localization and filtering

Acquired dSTORM stacks were processed by Thunderstorm, a Fiji plugin for PALM and STORM data analysis. At first, we set the properties of acquisition by the "Camera setup" menu: pixel size = 162 nm, Photoelectrons per A/D count: 0.9, Base level: 100 counts. Then, we carried out the localization algorithm ("Run analysis"), setting the following parameters: a) pre-filter: wavelet filter (B-spline), scale: 2, order: 3; b) approximate localization of molecules by local maximum method with threshold 3x standard deviation of the wavelet filter and 8-neighbourhood connectivity; c) sub-pixel localization by the Integrated Gaussian method, performing least-squares fitting with initial sigma 1.6 pixels and fitting radius 3 pixels. Eventually, we cleaned the obtained results from drift and those localizations not strictly lying on the focal plane by the following post-filtering algorithm: a) drift correction by correlation (1-5 points); b) removal of localizations with sigma >180 nm AND uncertainty < 30 nm.

Image rendering of single localization maps (with pixel size: 32 nm) was obtained by using gaussian functions peaked on each localization and with sigma corresponding to the relevant localization precision.

Ripley's analysis

A custom-made MATLAB code was developed to compute Ripley's H function analysis in an unlimited a priori rectangular area. At first, Ripley's *K(r)* function was calculated according to:

$$K(r) = \frac{A}{N^2} \sum_{i,j} \quad \delta_{i,j} \quad [1]$$

Where A is the area of the selected rectangular ROI in the dSTORM image, N is the number of total localizations in the area, *r* is the spatial variable (radius) that determines the *K* function, and $\delta_{i,j}$ = 1 if the distance between the i-th and j-th localizations is less

than r, otherwise $\delta_{i,j} = 0$.

K(r) was then transformed in Ripley's function *H(r)*, which measures the spatial randomness of the localization map.

$$H(r) = \sqrt{\frac{K(r)}{\pi}} - r \qquad [2]$$

According to its definition, *H(r)* must be zero when the localizations are distributed isotropically, and positive when particles are clustering. The code computed *K(r)* and *H(r)* for $0 < r \leq 1$ μm. In order to avoid boundary problems, the code computes distances only from *i-th* localizations (eq.1) that have ≥1 μm distance from the ROI edges.

Density-Based Algorithm for Discovering Clusters in Large Spatial Databases with Noise (DBSCAN) analysis

DBSCAN is a density-based spatial clustering method that requires two parameters for detecting and segmenting the clusters in SMLM data, namely a neighborhood radius ε and the minimum number of localizations/points (*MinPts*) within ε to qualify as a cluster ([32]). DBSCAN hierarchical cluster analysis was carried out on the same ROIs used for Ripley's analysis. We set 20 nm as the core radius and 25 as the minimum number of localizations within the radius to qualify as a cluster. These values correspond to a minimum of 2 "cluster" localizations in a 10x10 nm square for a cluster, which corresponds to the Nyquist frequency for ~10 nm localization precision. DBSCAN analysis was performed by the LocAlization Microscopy Analyzer software (LAMA), available for download at http://share.smb.uni-frankfurt.de/index.php/software-menue/lama. The output of the analysis was a table listing all identified clusters: their area, their radius, and the number of embedded localizations.

Graphics and statistics

Graphs were prepared using Prism 7 (GraphPad) and IgorPro8 (Wavemetrics) software. Data are shown as the mean +/- SEM. Statistical analysis was performed by Prism 7 (GraphPad).

RESULTS

Selection of NSCLC cell line model

From literature data, it is known that activation of EGFR is positively associated with the activation of PD-L1 in NSCLC cells. [33]. Accordingly, we set out to inspect the expression level of a family of NSCLC cell lines with different mutation patterns of the *EGFR* gene, namely H1975, H3255, H1650, PC9, and HCC827 [34]. Of note, these cell lines were reported to be characterized by a noticeable transcription level of the *PD-L1* gene as assessed by the cancer cell line encyclopedia (Table 1).

Table 1: *Mutation pattern and transcription level of several EGFR-mutated NSCLC cell lines from the cancer cell line encyclopedia (https://sites.broadinstitute.org/ccle/)*

	H1975	H3255	H1650	HCC827	PC9
EGFR mutation	L858R/T790M	L858R	746-750del	746-750del	746-750del
mRNA(rpkm)	$5.41 \cdot 10^5$	$7.03 \cdot 10^5$	$1.74 \cdot 10^5$	$1.74 \cdot 10^5$	$2.09 \cdot 10^5$

The actual expression level in living cells was evaluated by flow cytometry by leveraging an anti-PD-L1 which targets an extracellular antigen of PD-L1 and avoids cell permeabilization. . Analysis of the histograms obtained from flow cytometry revealed the positive immunostaining of PD-L1 as compared to the negative control and autofluorescence (**Figure 1a**). Median fluorescence values across the several cell lines hinted clearly at a much larger expression of membrane PD-L1 in HCC827 (**Figure 1b**). Accordingly, we selected HCC827 as our cell model to enable the largest sensitivity in the subsequent imaging experiments.

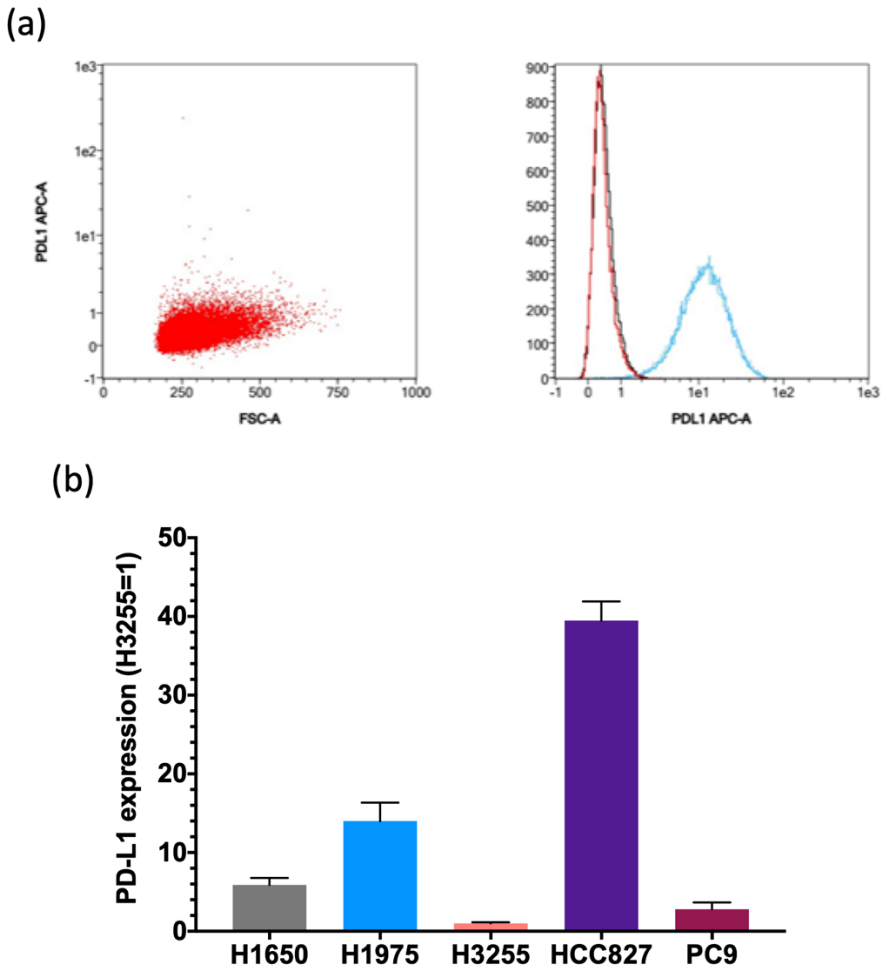

Figure 1. Selection of the NSCLC cell line model with highest expression of PD-L1. (a) Dot plot and histogram presentation of PD-L1 expression on ~~in~~ HCC827. Histograms: autofluorescence (black), IgG Isotype Control (red), positively immuno-stained cells (blue). (b) Relative PD-L1 expression of lung cancer cell lines (#3 measurements per cell line).

Imaging of membrane PD-L1 and colocalization with lipid raft markers

Membrane PD-L1 was observed in HCC827 cells by confocal and TIRF microscopy by indirect immunofluorescence by using Alexa647 as a fluorescent reporter (**Figure 2**). To provide selective membrane staining, cells were not permeabilized before immunolabeling. The high selectivity of PD-L1 staining at the plasma membrane level was confirmed by collecting confocal images at different focal planes and optically reconstructing the observed cells (**Figure 3**).

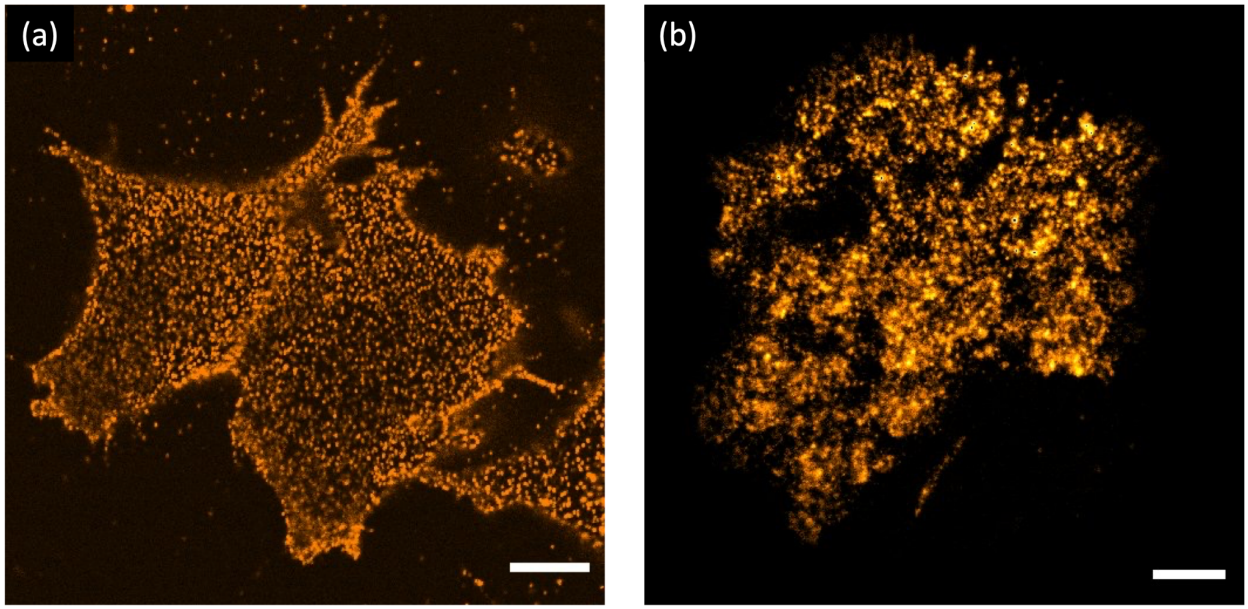

Figure 2. Confocal (a) and TIRF (b) images of HCC827 cells immunostained for PDL1 (orange). Scale bar: 10 μm.

Interestingly, membrane PD-L1 was organized mostly into a heterogeneous distribution of foci, possibly representing aggregate structures (**Figure 2**). To investigate whether these aggregates could be related to membrane lipid rafts, we carried out colocalization studies of PD-L1 and two raft markers. More specifically, as raft hallmarks, we used transiently expressed glycosylphosphatidylinositol (GPI) fused to EGFP (GPI-EGFP) or Caveolin-1 fused to EGFP (Cav-1-EGFP). GPI is a common anchoring motif of several proteins to the cell membrane and GPI-anchored proteins were shown to reside mostly in lipid rafts [17, 35]. Caveolin-1 is the hallmark of caveolae, flask-like invaginations of the plasma membrane responsible for "caveolar" endocytosis and that are considered to be a subset of lipid membrane rafts [24, 36]. PD-L1 was again immunostained by Alexa647, which is characterized by almost no emission overlap with EGFP, thereby avoiding spurious colocalization effects due to spectral overlap. TIRF microscopy was adopted to provide selective imaging of the basal membrane.

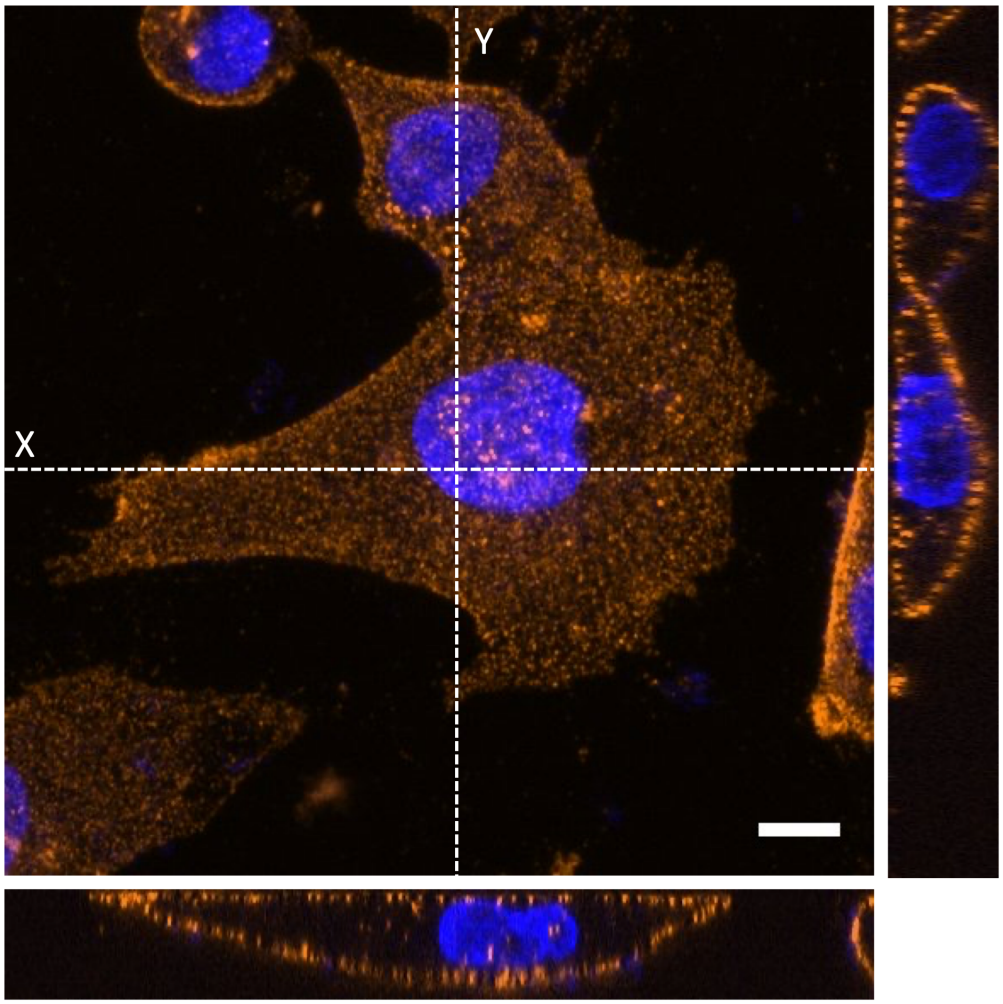

Figure 3. Spatial distribution of PDL1 on HCC827 cells by high magnification confocal microscopy. Central image is a maximum projection of a stack of images collected over 13.4 μm along the Z-direction. Left and bottom panels show the YZ and XZ images collected by sectioning along the Y and X dashed lines, respectively. Blue: Hoechst, orange: PDL1. Scale bar: 10 μm.

The large and visible yellow patches in the two-color image showed that the green (GPI-EGFP or Cav-1-EGFP) and red channels (PD-L1) were significantly colocalized (**Figure 4**). This pattern was quantitatively confirmed by the calculation of the images of Pearson's coefficient R (**Figure 5**). R measures the stoichiometric correlation between the two fluorescent partners as a proxy of their functional association [37]. We found out <R>=0.33±0.06 (average±SEM, #10 cells) for the colocalization with GPI-EGFP, and <R>=0.28±0.05 for the colocalization with Cav-1-EGFP (#11 cells). These values were

significant as compared to negative control of colocalization made of cells expressing either GPI-EGFP or Cav-1-EGFP and immunostained in absence of the primary anti-PD-L1 antibody (<R>=0.08±0.02, #6 cells, **Figure 5**).

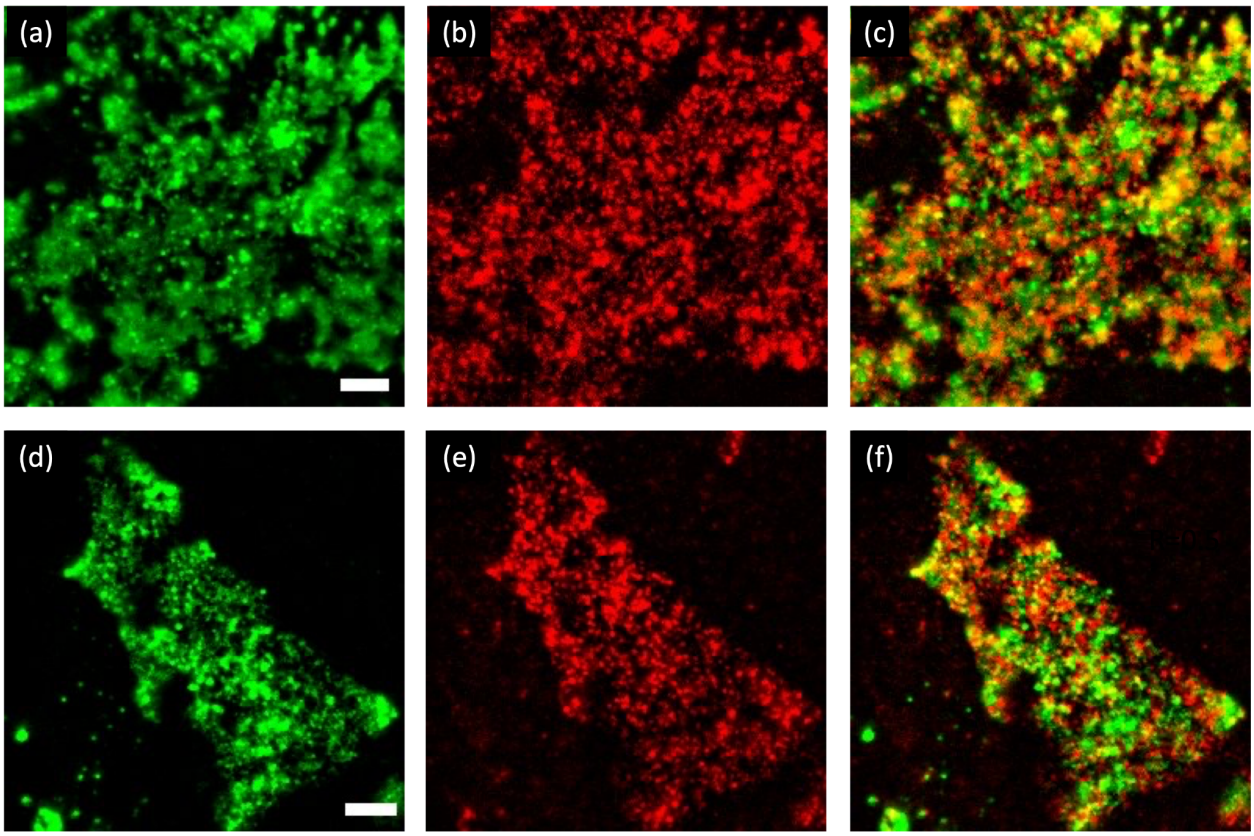

Figure 4. Localization of PDL1 into raft-enriched regions assessed by TIRF microscopy in HCC827 cells. (a) TIRF image of transiently expressed GPI-EGFP (green). (b) TIRF image of immunostained PDL1 (red). (c) Overlap of image (a) and (b): Pearson's coefficient R=0.63. (d) TIRF image of transiently expressed Caveolin-1-EGFP (green). (e) TIRF image of immunostained PDL1 (red). (f) Overlap of image (d) and (e): Pearson's coefficient R=0.5. Scale bar: 5 μm.

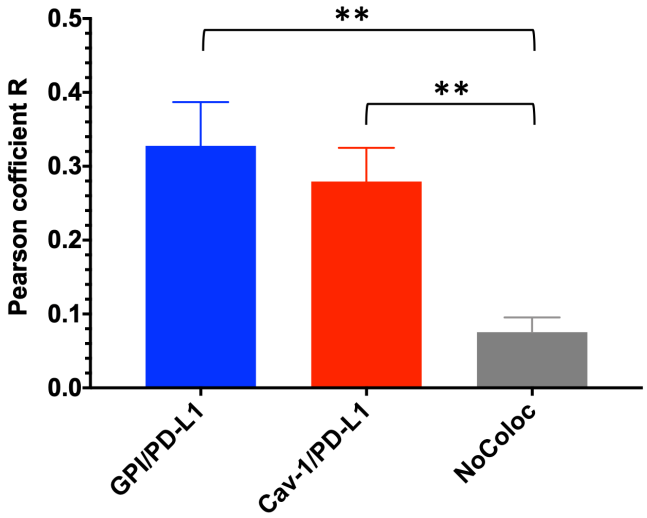

Figure 5. Pearson coefficients (average±SEM) for GPI-EGFP/PD-L1 (blue) and Cav-1-EGFP/PD-L1 (red) colocalization assessed on TIRF images. Comparison is with a no-colocalization (dark grey) control deterrmined on cells transfected with GPI-EGFP or Cav-1-EGFP and immunostained in absence of the primary antibody targeting PD-L1; t-test: $p \leq 0.01$ (**).

Single-molecule localization microscopy of PD-L1 on the basal membrane of resting and cholesterol-deprived cells

The nanoscale spatial arrangement of PD-L1 on the basal membrane of physiological (Physio) HCC827 cells was investigated by dSTORM in TIRF mode. Again, cells were not permeabilized before immunostaining to avoid spurious signals from cytoplasmic PD-L1. By collecting 20-40 k frames we were able to identify 500,000-2,000,000 single molecules. A qualitative inspection of the single molecule maps confirmed the heterogeneous spatial distribution of PD-L1 on the basal membrane previously observed by confocal microscopy (**Figure 6a**) and revealed the existence of nanoscale aggregates (**Figure 6b**). The average localization precision of single molecule maps was 7.2±0.5 nm (average±SEM, #12 cells, **Figure 7a**).

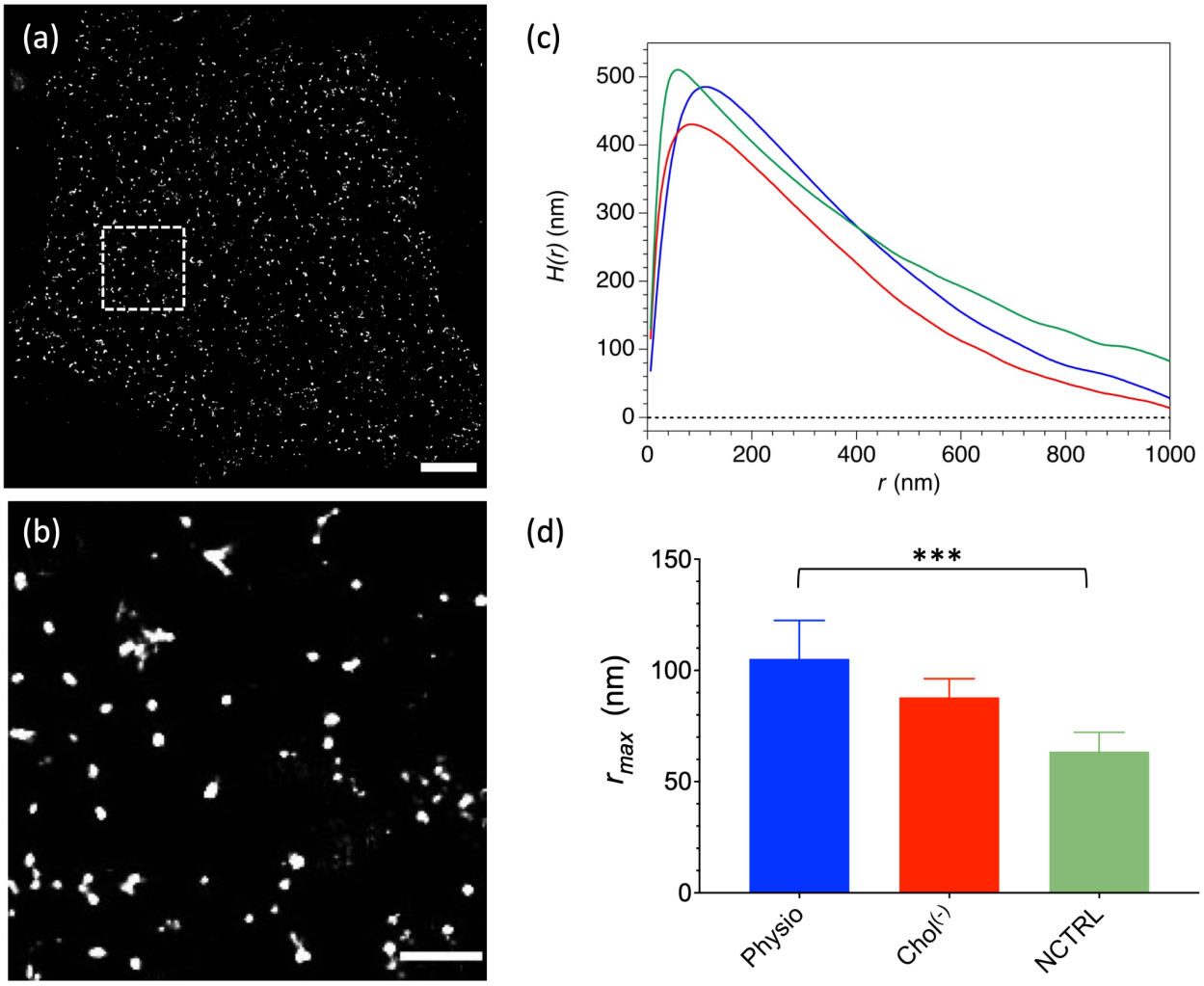

Figure 6. PD-L1 by dSTORM in TIRF mode. (a) Gaussian rendering of dSTORM map of one HCC827 cell membrane immunostained for PD-L1. (b) Zoom of the region enclosed by the white dashed square in panel (a). (c) Plot of Ripley's function *H(r)* for one HCC827 in physiological condition (Physio, blue), after cholesterol-depletion (Chol$^{(-)}$, red), and immunostained only by the secondary antibody (NCTRL, green); the dashed black line for *H(r)*=0 refers to isotropic distribution of molecules. (d) Histogram of Ripley's r_{max} for Physio (# 12 cells), Chol$^{(-)}$ (#8 cells), and NCTRL (#4 cells); Anova, p=.0001 (***). Scale bar: 10 µm (a), 1 µm (b).

Cholesterol depletion by MBCD is a classical way to perturb membrane rafts and modulate the residence of embedded proteins. Accordingly, we exposed HCC827 cells to MBCD for 1h before fixation and immunostaining (Chol$^{(-)}$ cells). Neither confocal (**Figure 7b**), nor dSTORM **(**Figure 7c) imaging showed that cholesterol depletion changed the

heterogeneous aggregate morphology of PD-L1 on the cell membrane. Of note, cholesterol depletion led to a ~51% decrease of the fluorescence due to PD-L1 (**Figure 7d**), albeit this compromised negligibly (+1.7 nm) the localization precision for Physio cells (**Figure 7a)**. Yet, the significant fluorescence loss suggested that the MBCD-induced raft disruption strongly affected PD-L1 stabilization on the cell membrane.

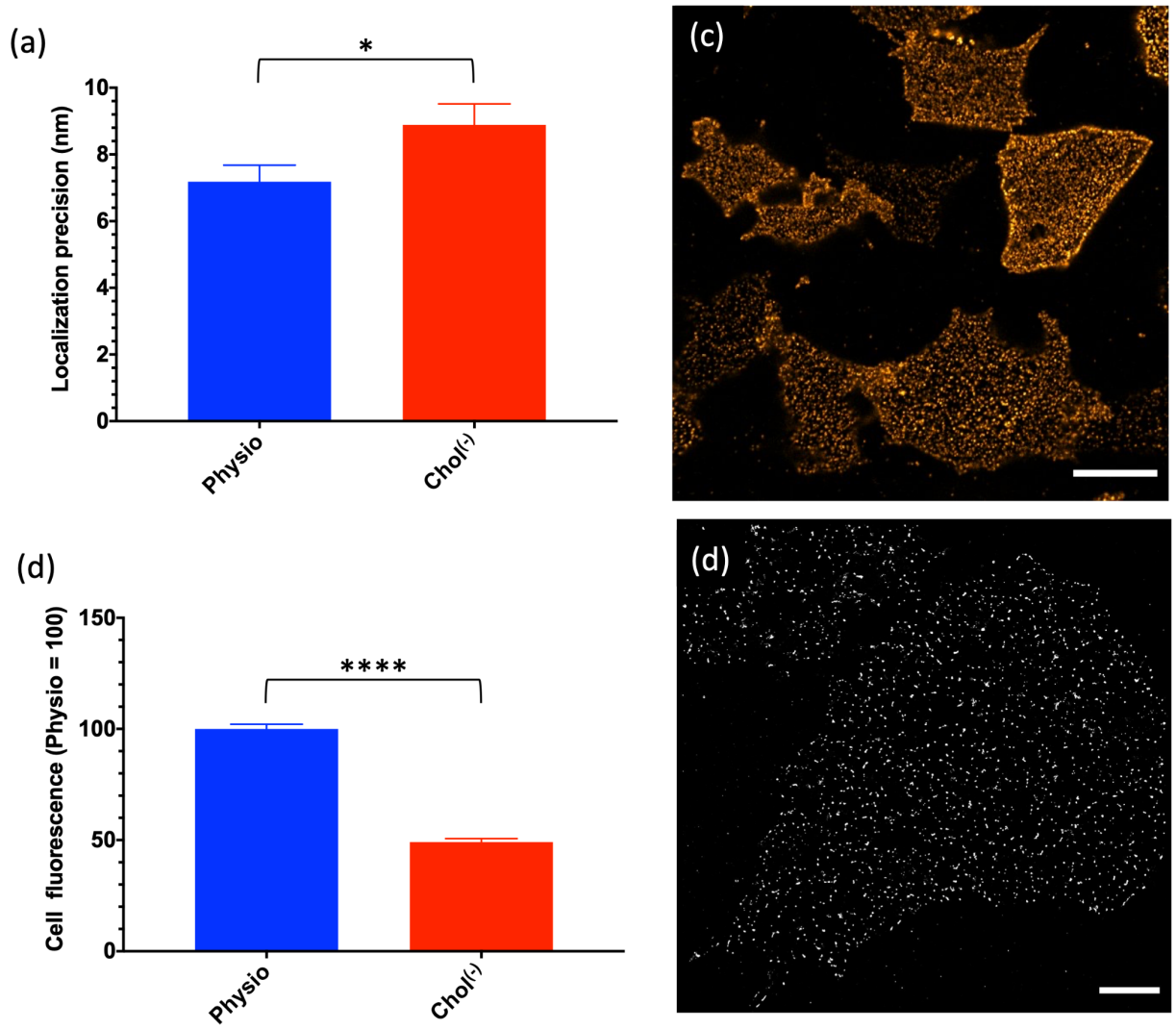

Figure 7. Effect of cholesterol depletion on HCC827 cells. (a) Average localization precision of dSTORM measurements; *p*=0.046 (*). (b) Confocal image of undepleted (Physio) HCC827 cells immunostained for PDL1 (orange scale). (c) Gaussian rendering of dSTORM map of cholesterol-depleted (Chol$^{(-)}$) HCC827 cells immunostained for PDL1 (grayscale). (b) Average cell fluorescence; p<0.0001 (****). Scale bar: 20 µm (b), 5 µm (c).

Ripley's cluster analysis of PD-L1 on the cell membrane

A first quantitative description of the nanoscale organization of PD-L1 was provided by Ripley's cluster analysis on dSTORM data. Ripley's method leverages a second-moment property of the single molecule spatial map to perform a statistical test between the actual point distribution and that associated with the isotropic dispersion of molecules in space ([32]). More specifically, Ripley's method calculates a global function $H(r)$ for increasing distances r from every single molecule in the xy image plane: $H(r)>0$ indicates clusterization, $H(r)=0$ indicates a uniform distribution of molecules, and $H(r)<0$ indicates spatial dispersion of molecules. The r_{max} value corresponding to the maximum of $H(r)$ is a proxy of cluster size ([38, 39]).

By Ripley's method, in the interval r = 0-1,000 nm we analyzed Physio (12 cells), Chol$^{(-)}$ (8 cells), and a negative control dataset (NCTRL, 4 cells) constituted by cells immunostained with only the secondary antibody. For each cell, the calculus of $H(r)$ was carried out in a large region of interest (>8x8 μm) to afford a representative result of the membrane distribution of PD-L1. In all cases, $H(r)$ grew sharply within the first 100 nm, reached a maximum, and slowly declined afterwards, suggesting the existence of nanoscale clusters (Figure 6c). We found out r_{max} = 105±5 nm (average±SEM) for Physio, r_{max} = 88±3 nm for Chol$^{(-)}$, and r_{max} = 63±4 nm for NCTRL cells (Figure 6d) and Anova test indicated statistical differences among the average r_{max} values ($p=1\cdot10^{-4}$). Given the large variability in the localization density between the samples (Max-Min: Physio 3,530-380 loc/μm^2 , Chol$^{(-)}$ 4,460-414 loc/μm^2 , NCTRL 174-83 loc/μm^2), we also verified if the emitter density could bias Ripley's analysis. Accordingly, we compared $H(r)$ between an actual dataset with 3,200 emitters/μm^2 and those obtained therefrom by removing the 85% of identified emitters either randomly one at a time (to mimic a generalized loss of localization density) or as random blocks of 100 sequential emitters (to remove localizations of the same group of molecules, *vide infra*). The final coordinate-based data did not display any significant difference $H(r)$ from the denser dataset (supplementary information, §1).

Owing to the partially reversible bright-dark photoconversion process of the Alexa647 fluorophore, a single photoactivated molecule may appear -and be localized- in several sequential images ("*on*" frames), then disappear for a while ("*off*" frames), re-appear and be localized again, and finally bleach completely. This leads to a substantial overcounting of blinking emitters and hampers a correct estimate of the real fluorophore density inside and outside the clusters. To correct for this, we combined all molecules (taking the average of their positions and the sum of their intensities) which blinked *off* for ≤10 consecutive frames and whose relative distance in adjacent frames was less than 40 nm, as we found these parameters were able to fully discriminate a repeated localization from those of two distinguishable emitters (supplementary information, §2). Ripley's analysis of the "merged" coordinate-based data afforded ~10 nm larger r_{max}, albeit a nearly linear correlation with unmerged r_{max} was observed (supplementary information, Figure S4), which conserved the statistical difference among Physio, Chol$^{(-)}$, and NCTRL (Anova: $p=7\cdot10^{-4}$). We can attribute the larger r_{max} values to the removal of repeated localizations that clusterize on a spatial scale similar to the SMLM localization precision, i.e. ~10 nm.

Density-based cluster analysis of PD-L1 on the cell membrane

To investigate further the nanoscale arrangement of PD-L1, we carried out a Density-Based Spatial Clustering of Applications with Noise (DBSCAN) analysis on the merged dSTORM data by observing the same ROIs where Ripley's functions were calculated. DBSCAN is a hierarchical clustering method that sorts localizations into clusters based on the local density and it can connect cluster regions of all kinds of shape ([32]). DBSCAN afforded spatial maps of clusters (Figure 8a), from which the area and the equivalent radius (r_c) could be calculated, as well as the number of localizations per cluster n_c.

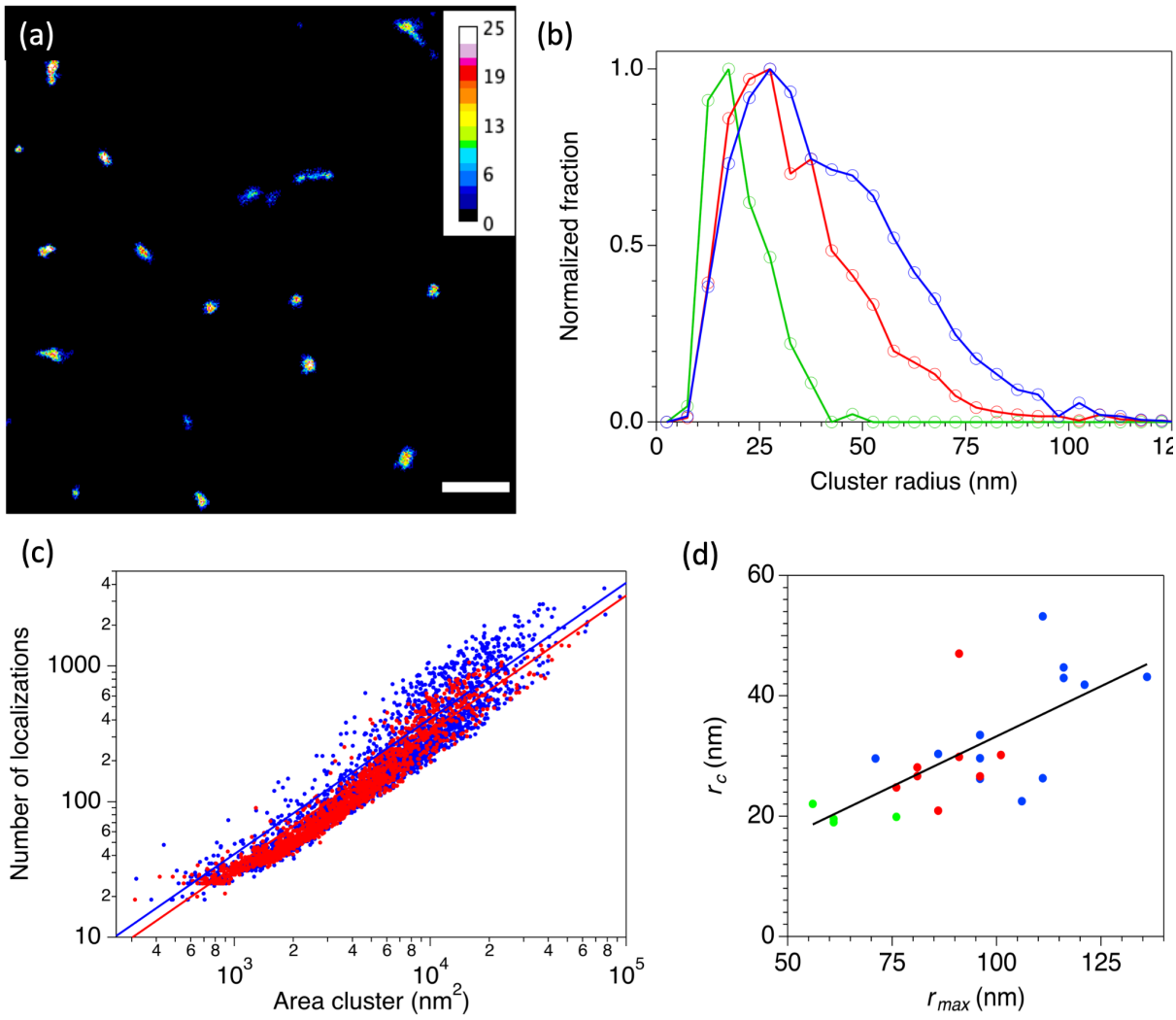

Figure 8. PD-L1 cluster analysis by DBSCAN. (a) DBSCAN map of clusters in a 4x4 μm membrane region of a HCC827 cell; the pseudocolor scale refers to the number of localizations in each 10x10 nm pixel. (b) Cluster radius (r_c) normalized distribution of Physio (blue, # 12 cells), Chol$^{(-)}$ (red, #8 cells), and NCTRL (green, #4 cells). (c) Plot of cluster localizations (n_c) *vs.* cluster area (A_c) for Physio (blue) and Chol$^{(-)}$ (red) datasets; lines represent linear fittings to retrieve cluster densities (ϱ_c). (d) Plot of DBSCAN r_c *vs* Ripley's r_{max}; values are correlated with R^2=0.5 (black line is the linear fit of data). Scale bar: 500 nm (a).

Both Physio and Chol$^{(-)}$ displayed polydisperse distributions of r_c, with tails extending above 100 nm (Figure 8b, blue and red traces). Of note, cholesterol depletion led to smaller aggregates and to a lower fraction f_c of emitters residing in clusters (Physio: $\langle r_c \rangle$=44.5±0.4 nm, f_c=54±7%; Chol$^{(-)}$: $\langle r_c \rangle$=37.0±0.4 nm, f_c=37±7%). Conversely, NCTRL was

characterized by rather small clusters ($\langle r_c \rangle$=22.5±0.6 nm) enclosing only a minor fraction of emitters (f_c=7±2%) (Figure 8b, green trace). This likely reflected a few non-specific aggregates of 2-3 secondary antibodies. Two-sample Kolmogorov-Smirnov test confirmed the statistical difference between the r_c distribution of Physio and Chol$^{(-)}$, as well as between NCTRL and each of the other two datasets (p<0.0001).

For each dataset, the plot of n_c *vs.* cluster area A_c was fitted to a linear equation:

$$n_i = \rho_c \cdot A_c \quad [1]$$

where ρ_c is the cluster density in the limit of zero area (Figure 8c). We found that Physio cells were characterized by a significantly higher ρ_c than Chol$^{(-)}$ (Physio: ρ_c=(4.11±0.03)·10^{-2} loc/nm^2; Chol$^{(-)}$: ρ_c=(3.32±0.02)·10^{-2} loc/nm^2; p<0.0001). The nearly unpredictable amplification of indirect immunofluorescence, i.e. heterogeneous multiple decorations of primary antibodies by polyfluorescent secondary antibodies, hampers the actual determination of PD-L1 densities in clusters. Yet, these data hint at a statistically reduced density of PD-L1 in clusters by ~20% alongside the dimensional shrinkage of the same aggregates.

Of note, for all cells, DBSCAN identified shorter cluster radii than Ripley's r_{max}. Previous studies pointed out that r_{max} falls between the radius and the diameter for a monodisperse system of clusters ([38, 39]). Also, being $H(r)$ a cumulative reporter of spatial heterogeneities, it is intrinsically very sensitive to cluster polydispersity, a feature that was common to all our datasets (Figure 8b). Nonetheless, the consistency of DBSCAN with the previous Ripley's analysis was confirmed by the good correlation between r_{max} and the average r_c for each cell (Figure 8d).

DISCUSSION

In the last few years, PD-L1 has become one of the most important therapeutic targets in oncology, on account of its remarkable standing as a cellular checkpoint of immune escape in many cancers. The molecular details of PD-L1 binding to its immune receptor PD-1 are well described. Yet, little is known about the arrangement of PD-L1 on the plasma membrane, a feature that is believed to play a role in the engagement of PD-1 and could represent a therapeutic target in itself. On account of the palmitoylation of Cys272, a residue located in the cytoplasmic tail of PD-L1, it has been speculated that PD-L1 may be engaged in the raft regions of the cell membrane. *In vitro* experiments seem to support this hypothesis, although nothing has been reported yet on the actual raft organization in living cells. In this work, we tackled this issue by a multi-scale imaging approach to characterize the PD-L1 functional morphology on the plasma membrane of integer cells. NSCLC is one kind of cancer where the role of the PD-L1/PD-1 immune checkpoint has higher relevance and is the subject of intense research to ameliorate present immunotherapy strategies. Accordingly, we focused our attention on NSCLC cell lines characterized by a high PD-L1 expression on the membrane. In this context, NSCLC cells bearing mutation on the *EGFR* gene have been reported to express medium-to-high levels of membrane PD-L1. Despite the expression of PD-L1, EGFR mutated tumors rarely respond to immunotherapy and EGFR mutations are considered a predictive marker of resistance to immune-checkpoint inhibitors in NSCLCs [40]. The molecular mechanisms underlying this phenomenon are still elusive to date. In the first part of this work, we screened a set of commonly used EGFR NSCLC cell lines to identify the one that would provide the highest expression of PD-L1. The rationale behind this approach was to enable high sensitivity in the subsequent imaging measurements, particularly those addressing the nanoscale arrangement of PD-L1. Cytofluorometry on living cells fluorescently immunolabeled on extracellular epitope(s) identified a very high expression for the HCC827 cell line compared to all the others. This line was therefore

adopted for the subsequent experiments.

Diffraction-limited imaging (max resolution: 250-300 nm) of immunostained cells by confocal or TIRF microscopy demonstrated a highly heterogeneous arrangement of mesoscale PD-L1 aggregates on the basal and apical plasma membranes. PD-L1 aggregates were found to colocalize strongly with two classical hallmarks of raft regions, glycosylphosphatidylinositol (GPI) and caveolin-1 (Cav-1). For this analysis we used transient expression of GPI-EGFP and Cav-1-EGFP, to induce the formation of larger raft regions as compared to the physiological condition. These findings clearly support the large engagement of PD-L1 in the raft regions. In keeping with this hypothesis, cholesterol depletion by MBCD led to significant loss of membrane PD-L1 in (still viable) cells, albeit the heterogeneous and mesoscale-aggregate morphology of PD-L1 on the membrane was maintained.

The nanoscale morphology of PD-L1 on the membrane was investigated by single-molecule localization microscopy applied to immunostained cells, using the dSTORM approach. This technique led to spatial maps of fluorophores, which act as proxies of PD-L1, super-resolved down to 7-10 nm. Ripley's and morphological (DBSCAN) clustering analysis clearly demonstrated the aggregation of PD-L1 in nanoclusters. The cluster radius distribution was within 100 nm, averaging near 45 nm, in good agreement with the observed size of lipid rafts. The observed cluster dimension was fully attributable to PD-L1 since non-specific aggregation of antibodies generated much smaller clusters (average radius ~23 nm). In physiological cells, DBSCAN showed that 45% of identified fluorophores did not belong to nanoclusters. Cholesterol depletion increased this figure to 63% together with a shrinking (~17%) of the average cluster radius. These changes were accompanied by a significant reduction in spatial density of fluorophores (-20%) in clusters upon cholesterol loss. Overall, these findings coherently support a model of PD-L1 partition between ordered (raft) and disordered regions of the plasma membrane, as also previously hypothesized from *in vitro* experiments. Engagement in rafts is

responsible for the nanoaggregate morphology of PD-L1. Cholesterol depletion removes rafts, forcing PD-L1 to the disordered bilayer phase where it is not clustered. Additionally, the remaining rafts have a smaller size and are less prone to accommodate PD-L1.

CONCLUSIONS

In conclusion, we characterized the relationships of PD-L1 with lipid rafts in the plasma membrane by taking advantage of a toolbox of fluorescence microscopy techniques operating at different spatial resolutions. As a cellular model, we selected the NSCLC *EGFR*-mutated cell line, HCC827, which we demonstrated to have an abundant plasma membrane expression of PD-L1. For the first time, the actual engagement of PD-L1 in the raft regions of a viable cell was demonstrated. On account of this, PD-L1 mainly arranges as nanostructured clusters (with <100 nm size) on the membrane. Consistently, this pattern is perturbed by cholesterol depletion, a well-known exogenous method to alter membrane rafts. We believe that these structural properties posit parallel functions in the context of PD-L1/PD-1 mediated immuno checkpoint and the immuno-oncology strategies to modulate it.

Author Contributions: BS, RB designed the study; BS, RB, SF, RD coordinated the research activity; MR, SC, TS, SC, VC, SB, IP, BS, RB performed research; MR, SC, BS, RB analyzed data; all authors wrote and revised the paper.

Funding: This research was supported by MIUR, Progetto di Ricerca di Interesse Nazionale, (bando PRIN 2017, Project n. 2017NR7W5K) awarded to Prof. Romano Danesi. All funding sources had no involvement in study design, collection, analysis, interpretation of data, writing the report; and decision to submit the article for publication.

Acknowledgments: Dr. Michele Oneto (IIT Nanophysics) are gratefully acknowledged for technical assistance and support.

BIBLIOGRAPHY

1. Kythreotou, A., et al., *Pd-L1.* Journal of Clinical Pathology, 2018. **71**(3): p. 189-194.
2. Cai, J.J., et al., *The Role Of PD-1/PD-L1 Axis In Treg Development And Function: Implications For Cancer Immunotherapy.* Oncotargets and Therapy, 2019. **12**: p. 8437-8445.
3. Chen, L.P. and D.B. Flies, *Molecular mechanisms of T cell co-stimulation and co-inhibition.* Nature Reviews Immunology, 2013. **13**(4): p. 227-242.
4. Chen, J., et al., *Regulation of PD-L1: a novel role of pro-survival signalling in cancer.* Annals of Oncology, 2016. **27**(3): p. 409-416.
5. Hudson, K., et al., *The Extrinsic and Intrinsic Roles of PD-L1 and Its Receptor PD-1: Implications for Immunotherapy Treatment.* Frontiers in Immunology, 2020. **11**.
6. Esfahani, K., et al., *A review of cancer immunotherapy: from the past, to the present, to the future.* Current Oncology, 2020. **27**: p. S87-S97.
7. Bai, R.L., et al., *Mechanisms of Cancer Resistance to Immunotherapy.* Frontiers in Oncology, 2020. **10**.
8. Reck, M., J. Remon, and M.D. Hellmann, *First-Line Immunotherapy for Non-Small-Cell Lung Cancer.* Journal of Clinical Oncology, 2022. **40**(6): p. 586-+.
9. Mazieres, J., et al., *Immune checkpoint inhibitors for patients with advanced lung cancer and oncogenic driver alterations: results from the IMMUNOTARGET registry.* Annals of Oncology, 2019. **30**(8): p. 1321-1328.
10. Escors, D., et al., *The intracellular signalosome of PD-L1 in cancer cells.* Signal Transduction and Targeted Therapy, 2018. **3**.
11. Zak, K.M., et al., *Structural Biology of the Immune Checkpoint Receptor PD-1 and Its Ligands PD-L1/PD-L2.* Structure, 2017. **25**(8): p. 1163-1174.
12. Yang, Y., et al., *Palmitoylation stabilizes PD-L1 to promote breast tumor growth.* Cell Research, 2019. **29**(1): p. 83-86.
13. Wen, M.R., et al., *PD-L1 degradation is regulated by electrostatic membrane association of its cytoplasmic domain.* Nature Communications, 2021. **12**(1).
14. Yao, H., et al., *Inhibiting PD-L1 palmitoylation enhances T-cell immune responses against tumours.* Nature Biomedical Engineering, 2019. **3**(4): p. 306-317.
15. von Knethen, A. and B. Brune, *PD-L1 in the palm of your hand: palmitoylation as a target for immuno-oncology.* Signal Transduction and Targeted Therapy, 2019. **4**.
16. Yao, H., et al., *A peptidic inhibitor for PD-1 palmitoylation targets its expression and functions.* Rsc Chemical Biology, 2021. **2**(1).
17. Levental, I., M. Grzybek, and K. Simons, *Greasing Their Way: Lipid Modifications Determine Protein Association with Membrane Rafts.* Biochemistry, 2010. **49**(30): p. 6305-6316.
18. Levental, I., et al., *Palmitoylation regulates raft affinity for the majority of integral raft proteins.* Proceedings of the National Academy of Sciences of the United States of America, 2010. **107**(51): p. 22050-22054.
19. Lorent, J.H., et al., *Structural determinants and functional consequences of protein affinity for membrane rafts.* Nature Communications, 2017. **8**.
20. Lingwood, D. and K. Simons, *Lipid Rafts As a Membrane-Organizing Principle.* Science, 2010. **327**(5961): p. 46-50.
21. Kusumi, A., et al., *Hierarchical mesoscale domain organization of the plasma membrane.* Trends in Biochemical Sciences, 2011. **36**(11): p. 604-615.
22. Kusumi, A., et al., *Membrane mechanisms for signal transduction: The coupling of the meso-scale raft domains to membrane-skeleton-induced compartments and dynamic protein complexes.* Seminars in Cell & Developmental Biology, 2012. **23**(2): p. 126-144.

23. Sezgin, E., et al., *The mystery of membrane organization: composition, regulation and roles of lipid rafts.* Nature Reviews Molecular Cell Biology, 2017. **18**(6): p. 361-374.
24. Patel, H.H. and P.A. Insel, *Lipid Rafts and Caveolae and Their Role in Compartmentation of Redox Signaling.* Antioxidants & Redox Signaling, 2009. **11**(6): p. 1357-1372.
25. Martinez-Outschoorn, U.E., F. Sotgia, and M.P. Lisanti, *Caveolae and signalling in cancer.* Nature Reviews Cancer, 2015. **15**(4): p. 225-237.
26. Zhang, S., et al., *Palmitoylation of PD-L1 Regulates Its Membrane Orientation and Immune Evasion.* bioRxiv, 2021: p. 2021.10.17.464736.
27. Lelek, M., et al., *Single-molecule localization microscopy.* Nature Reviews Methods Primers, 2021. **1**(1): p. 39.
28. Diaspro, A. and P. Bianchini, *Optical nanoscopy.* Rivista Del Nuovo Cimento, 2020. **43**(8): p. 385-455.
29. Sauer, M. and M. Heilemann, *Single-Molecule Localization Microscopy in Eukaryotes.* Chemical Reviews, 2017. **117**(11): p. 7478-7509.
30. Zidovetzki, R. and I. Levitan, *Use of cyclodextrins to manipulate plasma membrane cholesterol content: evidence, misconceptions and control strategies.* Biochim Biophys Acta, 2007. **1768**(6): p. 1311-24.
31. Costes, S.V., et al., *Automatic and quantitative measurement of protein-protein colocalization in live cells.* Biophysical Journal, 2004. **86**(6): p. 3993-4003.
32. Khater, I.M., I.R. Nabi, and G. Hamarneh, *A Review of Super-Resolution Single-Molecule Localization Microscopy Cluster Analysis and Quantification Methods.* Patterns, 2020. **1**(3).
33. Zhang, N., et al., *The EGFR pathway is involved in the regulation of PD-L1 expression via the IL-6/JAK/STAT3 signaling pathway in EGFR-mutated non-small cell lung cancer.* International Journal of Oncology, 2016. **49**(4): p. 1360-1368.
34. Nishiyama, N., et al., *Morphometric and Cytomorphologic Characterization of EGFR-mutated Cancer Cells-Comparison Between Cultured Lung Cancer Cell Lines and Lung Adenocarcinoma Clinical Samples.* Diagnostic Cytopathology, 2016. **44**(9): p. 717-724.
35. Komura, N., et al., *Raft-based interactions of gangliosides with a GPI-anchored receptor.* Nature Chemical Biology, 2016. **12**(6): p. 402-U51.
36. Storti, B., et al., *Unveiling TRPV1 Spatio-Temporal Organization in Live Cell Membranes.* Plos One, 2015. **10**(3).
37. Adler, J. and I. Parmryd, *Quantifying Colocalization by Correlation: The Pearson Correlation Coefficient is Superior to the Mander's Overlap Coefficient.* Cytometry Part A, 2010. **77A**(8): p. 733-742.
38. Kiskowski, M.A., J.F. Hancock, and A.K. Kenworthy, *On the Use of Ripley's K-Function and Its Derivatives to Analyze Domain Size.* Biophysical Journal, 2009. **97**(4): p. 1095-1103.
39. Ruan, Y., et al., *The Accuracy of Determining Cluster Size by Analyzing Ripley's K Function in Single Molecule Localization Microscopy.* Applied Sciences-Basel, 2019. **9**(16).
40. Borghaei, H., et al., *Nivolumab versus Docetaxel in Advanced Nonsquamous Non-Small-Cell Lung Cancer.* New England Journal of Medicine, 2015. **373**(17): p. 1627-1639.